SPH in spherical and cylindrical coordinates

M. Omang [a,b,*], S. Børve [c], J. Trulsen [b]

[a] *Norwegian Defence Estates Agency, P.O. Box 405 Sentrum, N-0103 Oslo, Norway*
[b] *Institute of Theoretical Astrophysics, P.O. Box 1029 Blindern, N-0315 Oslo, Norway*
[c] *Centre of Mathematics for Applications, P.O. Box 1053 Blindern, N-0316 Oslo, Norway*

Abstract

New kernel functions for spherically, planar and cylindrically symmetric problems are developed, based on the fundamental interpolation theory of SPH. The Lagrangian formalism is used to derive the corresponding set of modified SPH equations of motion. The results show good agreement both with analytical and numerical results, in the case of the Sod shock tube test, the Noh infinite shock problem, and the Sedov point explosion test. The formulation has also been included in a 3D cylindrically symmetric problem of two colliding spherical shocks. For this latter problem, the results are presented allowing both a constant and a variable resolution. The results clearly demonstrate the capability of the new formulation to solve the singularity problem at the symmetry axis.
© 2005 Elsevier Inc. All rights reserved.

1. Introduction

Smoothed particle hydrodynamics (SPH) is a Lagrangian numerical method based on a description, where a set of particles are used to simulate a continuous fluid flow. The method was originally developed for a Cartesian coordinate system, and only limited effort has been put into developing an SPH code in cylindrical or spherical coordinates that take advantage of existing cylindrical or spherical symmetries. SPH formulations for cylindrically symmetric systems are given in [1,2]. These descriptions are derived based on the standard Cartesian kernel function which is multiplied by the inverse radius and renormalized. The equations of motion are, except for the radial dependence left unaltered. Similar approaches are presented in [3,4], although alternative kernel functions are applied.

In the field of material modeling, efforts have been put into handling impact problems with SPH. In this connection, a solution to the development of a cylindrical description in SPH is presented [5]. Equations of motion in cylindrical coordinates are derived by making a change of coordinates and performing an axi-symmetric

---

* Corresponding author. Tel.: +47 22 857527; fax: +47 22 856505.
  E-mail address: momang@astro.uio.no (M. Omang).

averaging of the equations of motion formulated in Cartesian coordinates. The averaging is performed assuming an infinite range Gaussian kernel function. Practical SPH calculations thus require the introduction of an arbitrary cut-off at finite range. The method is found applicable to impact type problems. In solving one of the more demanding numerical tests in hydrodynamics, the Noh infinite shock problem [6], however, the results reveal problems in obtaining correct density levels. Problems are also reported in the region close to the origin. A later paper by the same group presents an improved solution to the same problem [7], in which a dual interpolation point technique is introduced. In this approach, one half of the interpolation points (particles) are constructed to carry stress, velocity gradients, and other derived field variables while the other half in a staggered fashion carries velocity information. The new description shows a distinct improvement of the shock capturing ability, though the post-shock density level is still somewhat under-estimated.

An alternative description of the axi-symmetric problem in cylindrical coordinates is presented in [8]. Here the Lagrangian formalism is used to formulate a set of equations of motion in which density ρ is replaced by a cylindrical density $\eta = 2\pi r \rho$. In these equations, the kernel function is replaced by symmetric one-dimensional functions in either r or z coordinates. The results presented for the cylindrical Sod shock tube problem [9] show good agreement with the results obtained using an alternative numerical Lagrangian finite difference method. Unfortunately, however, numerical results are only presented for the region well removed from the symmetry axis $r = 0$. As the definition of the density may indicate, the description does not handle the situation in which $r \to 0$. Consequently, the code is not suited for solving the infinite shock problem as described in [6].

Modifications of the standard kernel functions to allow local anisotropy is performed by different groups. In [10], a Taylor expansion of the standard kernel function is used to construct a quartic smoothing function, whereas ellipsiodial kernels are used in [11].

In this paper, we present a different approach to spherically and cylindrically symmetric descriptions using SPH. In our approach, we make explicit use of the assumed symmetry in the fundamental interpolation formula to derive suitable kernel functions in the appropriate coordinate system. The kernel functions thus embed the particular symmetry of the problem. Equations of motion with the new kernel functions are derived making use of Lagrangian formalism.

In the next section, we give a short introduction to the fundamentals of SPH. For the spherically symmetric description, the solution is presented in Section 3. A new set of the equations of motion and some test results are given in Section 4. The new technique could also be applied to plane symmetric problems in a Cartesian coordinate description. The derivation of the planar description and some results using this description are presented in Section 5, followed by the cylindrical description in Section 6. In Section 7, results for a 3D cylindrically symmetric problem of two colliding spherical shocks are presented. For this problem, we present results obtained both with a constant resolution, and by making use of the full capability of our RSPH code [12], including both a stepwise constant h-profile and regularization. Finally, in Section 8, we give a short discussion and some concluding remarks.

2. Fundamentals of SPH

The SPH method [13] is based on interpolation theory, in which an arbitrary field function $F(\mathbf{r})$ (and its derivatives) is expressed in terms of its values at a set of disordered points. This is achieved by approximating the function $F(\mathbf{r})$ by its integral interpolant $\langle F(\mathbf{r}) \rangle$,

$$F(\mathbf{r}) \approx \langle F(\mathbf{r}) \rangle \equiv \int d\mathbf{r}' \, F(\mathbf{r}') W(\mathbf{r}' - \mathbf{r}, h) \tag{1}$$

and subsequently discretizing the integral. The kernel function, W, should normalize to unity and become a delta function in the limit where the characteristic smoothing length h approaches zero. The kernel function is usually chosen to be differentiable, non-negative and symmetric, $W(\mathbf{r}', \mathbf{r}; h) = W(|\mathbf{r}' - \mathbf{r}|, h)$. In Eq. (1), the integration is over the entire space. The choice of a kernel function with finite support is, however, essential in order to reduce the number of particle interactions and therefore code efficiency. For the subsequent discussion, the frequently used third-order B-spline function [14] in δ-dimensional space is our choice of "generic" kernel function,

$$W(\mathbf{r}', \mathbf{r}; h) = \mathscr{W}_\delta(q) \equiv \frac{1}{N(\delta)h^\delta} \begin{cases} 1 - \frac{3}{2}q^2 + \frac{3}{4}q^3, & 0 \leqslant q < 1, \\ \frac{1}{4}(2-q)^3, & 1 \leqslant q < 2, \\ 0, & 2 \leqslant q, \end{cases} \tag{2}$$

where $q = |\mathbf{r}' - \mathbf{r}|/h$ and the normalization factor $N(\delta) = \{\frac{3}{2}, \frac{7}{10}\pi, \pi, \frac{31}{70}\pi^2, \frac{3}{5}\pi^2\}$ for $\delta = 1, \ldots, 5$. Reasons for including spatial dimensions up to 5 will become clear during the subsequent discussion.

3. Spherically symmetric interpolation

For a spherically symmetric field quantity $F(\mathbf{r}) = F(r)$, the integral interpolant equation (1) reduces to

$$\langle F(r) \rangle = \int dr' \, r'^2 F(r') \int d\cos\theta \, 2\pi \mathscr{W}_3(q) \tag{3}$$

where $q = \sqrt{(r'-r)^2 + 4rr'\sin^2(\theta/2)}/h$ and θ is the angle between $\mathbf{r}'$ and $\mathbf{r}$. Since $h^2q \, dq = rr' \, d\cos\theta$, it follows that

$$\langle F(r) \rangle = \int dr' \, r'^2 F(r') W_{3S1}(r', r; h), \tag{4}$$

where the appropriate kernel function for the spherically symmetric problem is given by

$$W_{3S1}(r', r; h) = \frac{2\pi h^2}{r'r} \int_{|r'-r|/h}^{\min(2, (r'+r)/h)} q\mathscr{W}_3(q) \, dq. \tag{5}$$

In the notation chosen for the resulting kernel function, W_{3S1}, the first index, in this case 3, indicates the dimension δ of the starting "generic" kernel function $\mathscr{W}_\delta$. The following letter indicates the particular type of symmetry, here S for spherical, whereas the latter number, in this case 1, gives the dimension of the resulting kernel function. By noting that

$$2\pi h^2 \int q\mathscr{W}_3(q) \, dq = \frac{1}{h} \begin{cases} C(q) \\ D(q) \end{cases} \equiv \frac{1}{h} \begin{cases} q^2 - \frac{3}{4}q^4 + \frac{3}{10}q^5, & 0 \leqslant q < 1, \\ 2q^2 - 2q^3 + \frac{3}{4}q^4 - \frac{1}{10}q^5, & 1 \leqslant q < 2 \end{cases} \tag{6}$$

and defining $\sigma \equiv r/h$ and $\sigma' \equiv r'/h$, the kernel function W_{3S1} can be written in the form:

for $2 < \sigma' + \sigma$:

$$W_{3S1}(r', r; h) = \frac{1}{hr'r} \begin{cases} \frac{7}{10} - C(|\sigma' - \sigma|), & 0 \leqslant |\sigma' - \sigma| < 1, \\ \frac{8}{10} - D(|\sigma' - \sigma|), & 1 \leqslant |\sigma' - \sigma| < 2, \end{cases} \tag{7}$$

for $1 < \sigma' + \sigma \leqslant 2$:

$$W_{3S1}(r', r; h) = \frac{1}{hr'r} \begin{cases} -\frac{1}{10} + D(\sigma' + \sigma) - C(|\sigma' - \sigma|), & 0 \leqslant |\sigma' - \sigma| < 1, \\ D(\sigma' + \sigma) - D(|\sigma' - \sigma|), & 1 \leqslant |\sigma' - \sigma| < 2 \end{cases} \tag{8}$$

and for $\sigma' + \sigma \leqslant 1$:

$$W_{3S1}(r', r; h) = \frac{1}{hr'r} (C(\sigma' + \sigma) - C(|\sigma' - \sigma|)). \tag{9}$$

We take notice of the fact that $\partial W_{3S1}/\partial r' \neq -\partial W_{3S1}/\partial r$. In Fig. 1, the kernel function $W_{3S1}(r', r; h)$ is plotted as a function of $r' - r$ for different values of r. The asymmetry with $r' - r$ for a given r is an important property of W_{3S1} that will give rise to so-called "hoop force" effects in the subsequent equations of motion. The degree of asymmetry decreases with increasing r as the spherical symmetry gradually reverts to local plane symmetry. We note that $W_{3S1}(r', r; h)$ is invariant relative to an interchange of its two arguments r' and r. Furthermore, while $W(\mathbf{r}', \mathbf{r}; h)$ is $\mathscr{C}^2$-continuous, the kernel function for spherical symmetry W_{3S1} is $\mathscr{C}^3$-continuous. By construction, W_{3S1} is normalized for every r, that is,

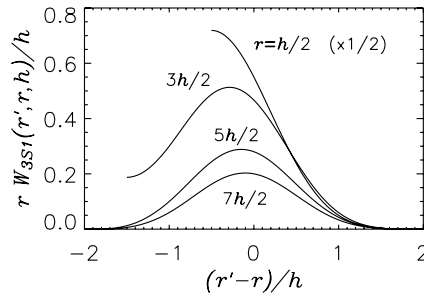$$\int dr' \, r'^2 W_{3S1}(r', r; h) = 1. \tag{10}$$

Fig. 1. Kernel function W_{3S1} for spherical symmetry.

4. Equations of motion in spherical SPH

To derive appropriate SPH equations of motion in a spherically symmetric coordinate system, we introduce

$$\mathrm{d}m' = \mathrm{d}r'\, r'^2 \rho(r') \tag{11}$$

as a new integration variable in Eq. (4). Apart from a factor 4π, $\mathrm{d}m'$ represents the infinitesimal mass in a spherical shell of radius r' and thickness $\mathrm{d}r'$. It is worth noting that this change of variable leads to an interpolation formula independent of the radius r, as the r dependence is found in the kernel function only. Next, the integral interpolant equation (4) is approximated by a summation interpolant,

$$F_i = F(r_i) \approx \sum_j m_j \frac{F_j}{\rho_j} W_{3S1}(r_j, r_i; h). \tag{12}$$

For the density, we thus obtain the following expression for particle i:

$$\rho_i \approx \sum_j m_j W_{3S1}(r_j, r_i; h). \tag{13}$$

Eq. (13) represents the continuity equation in the SPH model. Furthermore, we require the position r_i and velocity v_i of particle i to vary in time according to

$$\frac{\mathrm{d}r_i}{\mathrm{d}t} = v_i. \tag{14}$$

An alternative formulation for Eq. (14), is the XSPH method [15], in which an additional term is added to Eq. (14), representing a velocity difference averaging in the particle neighborhood.

The momentum equation follows by introducing the particle Lagrangian [16–18]

$$L = \sum_j m_j \left(\frac{1}{2} v_j^2 - e(\rho_j, s_j) \right), \tag{15}$$

with the internal energy density $e(\rho, s)$, given as a function of density ρ and entropy s. The momentum equation for isentropic flow resulting from the Lagrangian (15) is then

$$m_i \frac{\mathrm{d}v_i}{\mathrm{d}t} = -\sum_j m_j \frac{\partial e(\rho_j, s_j)}{\partial \rho_j} \frac{\partial \rho_j}{\partial r_i}. \tag{16}$$

Since

$$\frac{\partial \rho_j}{\partial r_i} = \sum_k m_k \frac{\partial}{\partial r_i} W_{3S1}(r_k, r_i; h)\delta_{ij} + m_i \frac{\partial}{\partial r_i} W_{3S1}(r_i, r_j; h), \tag{17}$$

and $(\partial e/\partial \rho)_s = P/\rho^2$ from the second law of thermodynamics, we find

$$\frac{\mathrm{d}v_i}{\mathrm{d}t} = -\sum_j m_j \left(\frac{P_i}{\rho_i^2} \frac{\partial}{\partial r_i} W_{3S1}(r_j, r_i; h) + \frac{P_j}{\rho_j^2} \frac{\partial}{\partial r_i} W_{3S1}(r_i, r_j; h) \right), \tag{18}$$

or, when the symmetry of the W_{3S1} function with respect to its two arguments r_j and r_i has been taken into account,

$$\frac{\mathrm{d}v_i}{\mathrm{d}t} = -\sum_j m_j \left(\frac{P_i}{\rho_i^2} + \frac{P_j}{\rho_j^2} + \Pi_{ij} \right) \frac{\partial}{\partial r_i} W_{3S1}(r_j, r_i; h). \tag{19}$$

In Eq. (19), we have also included the artificial viscosity Π_{ij} which is introduced to reduce numerical errors in computations of strong shock wave problems. So far we have made use of the standard form of the artificial viscosity in SPH [14] as derived from the artificial viscosity developed for finite difference methods [19].

The energy equation is derived by noting that

$$\frac{\mathrm{d}e_i}{\mathrm{d}t} = \frac{P_i}{\rho_i^2} \frac{\mathrm{d}\rho_i}{\mathrm{d}t}, \tag{20}$$

with

$$\frac{\mathrm{d}\rho_i}{\mathrm{d}t} = \sum_j m_j \left(v_j \frac{\partial}{\partial r_j} + v_i \frac{\partial}{\partial r_i} \right) W_{3S1}(r_j, r_i; h). \tag{21}$$

Thus,

$$\frac{\mathrm{d}e_i}{\mathrm{d}t} = \sum_j m_j \left(\frac{P_i}{\rho_i^2} + \frac{1}{2} \Pi_{ij} \right) \left(v_j \frac{\partial}{\partial r_j} + v_i \frac{\partial}{\partial r_i} \right) W_{3S1}(r_j, r_i; h). \tag{22}$$

Together with the equation of state

$$P_i = (\gamma - 1)e_i \rho_i, \tag{23}$$

where γ is the ratio of specific heats, Eqs. (13), (14), (19) and (22) constitute the equations of motion in the spherically symmetric case.

The conservation law properties of the equations of motion derived from a Lagrangian formalism are normally ascertained by considering the symmetry properties of the Lagrangian [17]. In the present case, we are dealing with equations formulated in curvilinear coordinates and an explicit problem symmetry imposed. For the spherically symmetric case, conservation of angular momentum is by assumption trivially satisfied. Conservation of radial momentum does not apply, while the invariance of L to a shift in time shows that energy $E = \sum_j v_j \partial L/\partial v_j - L = \sum_j m_j (\frac{1}{2} v_j^2 + e(\rho_j))$ is conserved.

4.1. Simple spherical tests cases

A simple test of the validity of the continuity and energy equations, Eqs. (13) and (22), can be performed by considering a controlled radial compression in a system with homogeneous mass and energy densities, and where the fluid velocity is everywhere and at all times given as $v = -r$. The continuity and energy equations for this case reduce to

$$\frac{\mathrm{d}\rho}{\mathrm{d}t} = -\frac{\rho}{r^2} \frac{\partial}{\partial r} (r^2 v) = 3\rho \tag{24}$$

and

$$\frac{\mathrm{d}e}{\mathrm{d}t} = \frac{P}{\rho^2} \frac{\mathrm{d}\rho}{\mathrm{d}t} = 3(\gamma - 1)e. \tag{25}$$

Both equations can be integrated. In Fig. 2, the relative errors $\Delta\rho/\rho$ (solid lines) and $\Delta e/e$ (dash-dotted lines) resulting from Eqs. (13) and (22) as compared with the analytical solution are plotted. The results are valid for
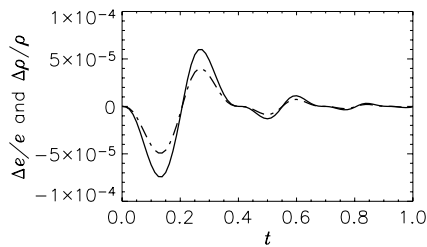
Fig. 2. Relative error in the density (solid lines) and energy (dash-dotted lines) for a spherical test of controlled radial compression.

any particle, independent of the initial radial distance r. The temporal variation in the relative error indicates the increased accuracy obtained as the interparticle separation is gradually reduced.

For a second and more complete test, we will use the SPH-based code RSPH [20,21] to consider the spherical version of the Sod shock tube problem [9]. A high pressure region of $p = 1.0$, $\rho = 1.0$ is separated from a low pressure region $p = 0.1, \rho = 0.125$ by a spherical membrane located at $r = 1.0$. The gas with a ratio of specific heats $\gamma = 1.4$, is initially at rest. Time is given relative to the instance when the membrane is removed. In the planar case, the numerical results are easily validated, by comparing with the analytical solution. In the spherical case, however, no analytical solution is available. We have therefore chosen to compare our results with the results obtained using a numerical 1D Riemann solver.

Fig. 3 shows the results obtained using RSPH (solid lines), for the density, pressure, internal energy and velocity in the radial direction. The particle number is approximately the same as the number of nodes used in the Riemann solver (dashed lines). The agreement with the Riemann solver results in Fig. 3 is good, even at the inner boundary ($r = 0$). The technique of using mirror particles [22,23] to handle boundary conditions, was only necessary at the outer boundary, as the kernel function automatically takes care of the boundary conditions at the origin.

Although RSPH allows the smoothing length to vary in time and space as a piecewise constant function, we have, for simplicity, used a constant smoothing length in this test and most of the other tests in this article. Another special feature of RSPH is the possibility of redefining the particle distribution at regular time intervals (particle regularization). A new set of particles are created in a regular configuration, based on the old particle distribution so as to ensure mass, energy and momentum conservation. A detailed description of
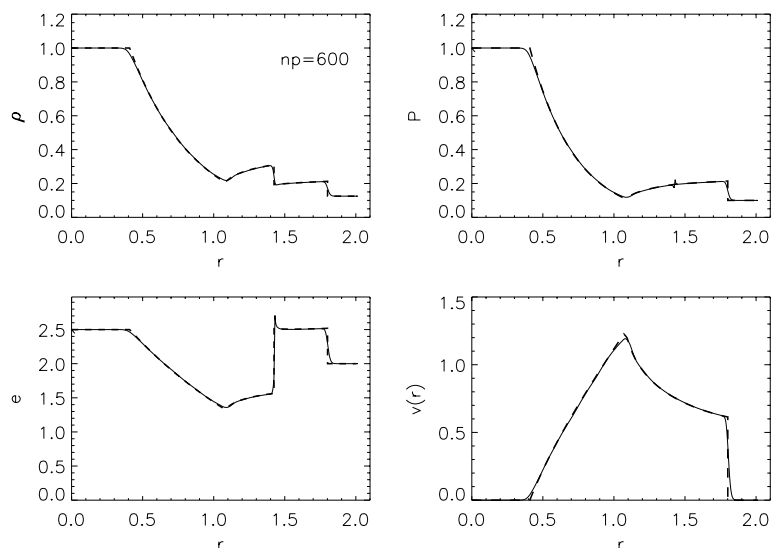

Fig. 3. Sod shock tube test in a spherically symmetric coordinate system at $t = 0.5$. Solid lines show the results obtained with RSPH (without particle regularization) and dashed lines show the results with the Riemann solver.
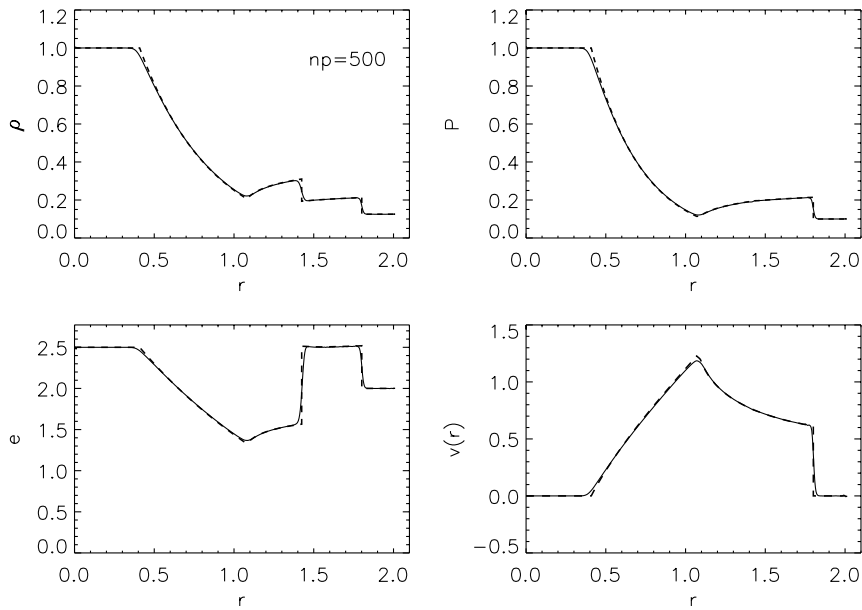
Fig. 4. Sod shock tube test in a spherically symmetric coordinate system at $t = 0.5$. Solid lines show the results obtained with RSPH (particle regularization applied) and dashed lines show the results with the Riemann solver.

the method is found elsewhere [12,20,24]. For the result presented in Fig. 3 particle regularization was not applied.

In Fig. 4, an identical test to that discussed in Fig. 3 is presented, this time, however, particle regularization has been applied. It is clear that the particle redefinition serves to reduce the noise. Both the spike in the energy profile and the characteristic blip in the pressure profile at the contact discontinuity, have been reduced as a result of the particle redefinition. In both cases, we deem the SPH results to be in good agreement with the Riemann solver results.

A reliable solution to the Sod problem without particle regularization can only be obtained with a smaller interparticle distance in the high pressure region. In the test presented in Fig. 3 we used 600 particles, with the particles in the high-pressure region distributed four times closer than in the low-pressure region. This is done to avoid substantial numerical errors in the rarefaction wave region due to increasing particle separation. With particle regularization this problem is reduced and in Fig. 4 we use 500 particles. Consequently, with particle regularization, less particles are necessary to achieve comparable resolution. For the remaining applications, we have therefore chosen particle regularization at regular time intervals, keeping the smoothing length constant.

The Noh problem [6] is a test well suited for numerical simulations in the planar, cylindrically and spherically symmetric cases, as there are analytical solutions available. A shock of infinite strength is created in a gas initially at rest. The ratio of specific heats is set to $\gamma = 1.4$. Driven by a constant velocity piston, the gas is brought to rest by a shock starting at the origin. It is a challenging test, in that the initial pressure and internal energy are set to zero. The initial density and velocity are set to $\rho = 1$ and $v = -1$. In the spherically symmetric case, the post-shock conditions are $\rho_+ = 64$, $v_+ = 0$, $p_+ = 64/3$ and $e_+ = 1/2$, whereas the pre-shock density given as a function of radius r is $\rho_- = (1 + t/r)^2$. At the position of the shock, determined from the relation $R_s = t/3$, the post-shock density is constant $\rho_-(R_s) = 16$. The constant shock speed is $V_s = \dot{R}_s = 1/3$.

In Fig. 5, we show the results obtained for the density, pressure, internal energy and radial velocity with RSPH (solid lines) compared to the analytical solution (dashed lines). The agreement is good and shows a significant improvement of the SPH results as presented by [5]. Except for the inner boundary, the two curves are difficult to distinguish. One of the topics studied in connection with the Noh problem [6] is the lacking ability of the von Neumann–Richtmyer artificial viscosity [19] to handle situations in which streaming gas
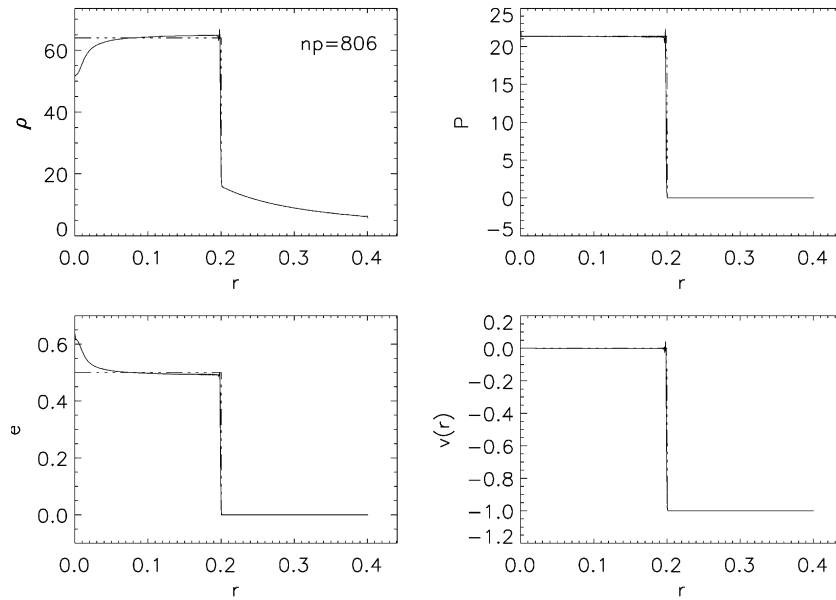
Fig. 5. Nohs numerical test for a spherically symmetric coordinate system at $t = 0.6$. Solid lines show the results obtained with RSPH and dashed lines show the analytical result.

is brought to rest at a rigid wall. The phenomena is referred to as excess wall heating. A solution to the excess wall heating problem is to introduce an artificial heat-conduction term. This term was first suggested by Noh [6], and has later been introduced in SPH methodology [13]. The energy rise and density dip observed in Fig. 5, are most likely a result of the excess wall heating problem. In the results presented here, the correcting artificial heat-conduction term is not included.

A separate parameter study of the characteristic parameters α and β in the formulation of the artificial U:/ ES/DTD501/YJCPH/994viscosity [25], showed that an increase in both α and β, would lead to the removal of the small overshoot at the shock front, as may be observed in Fig. 5. An additional effect, however, was the reduction of the overall pre-shock density level. We used $\alpha = 1$ and $\beta = 2$ in these computations. In our simulations with the smoothing length set to $h = .001$ and allowing two particles per h, there were 2000 particles distributed initially. As the computational domain is constantly reduced, the particle regularization ensures that only about 800 particles remain at $t = 0.6$.

As a final test of the spherically symmetric formulation, we present results for the Sedov point explosion. The analytical solution for a point explosion is given by Sedov [26], making the assumption that the atmospheric pressure relative to the pressure inside the explosion is negligible. The position of the shock as a function of time t, relative to the initiation of the explosion, is given as

$$R(t) = \left(\frac{et^2}{\rho_0}\right)^{1/(\delta+2)}, \tag{26}$$

with $\delta = 2$ and $\delta = 3$ for cylindrical and spherical geometry, respectively. The density in the undisturbed atmosphere is ρ_0, whereas e is a dimensionless energy. Behind the shock, we have the following properties:

$$\rho_2 = \frac{\gamma + 1}{\gamma - 1}\rho_0, \tag{27}$$

$$P_2 = \frac{2}{\gamma + 1}\rho_0 w^2, \tag{28}$$

$$v_2 = \frac{2}{\gamma + 1}w, \tag{29}$$

where the shock velocity

$$w(t) = \frac{dR}{dt} = \frac{2}{\delta + 2} \frac{R(t)}{t} \qquad (30)$$

is obtained from Eq. (26). The complete (and lengthy) analytical solution to the pressure, density and velocity profile behind the shock front can be found in [26].

In numerical simulations, energy deposition in a single point is difficult to tackle. A solution to the problem, first suggested by Brode [27,28], is to make use of the bursting balloon analogue. Rather than depositing the total energy in a single point, the energy is released into a balloon of finite volume V

$$e = \frac{(P - P_0)V}{\gamma - 1}. \qquad (31)$$

The energy release in a balloon of radius r_0 raises the pressure to the value,

$$P = \frac{3(\gamma - 1)e}{(\delta + 1)\pi r_0^{\delta}}. \qquad (32)$$

In the simulations, we assume that the undisturbed medium is at rest with a pressure $P_0 = 1.0 \times 10^{-5}$. The density is constant $\rho_0 = 1$, also in the pressurized region. In Fig. 6, we have plotted the results at $t = 0.05$ for density, pressure and velocity for an increasing number of particles. For simplicity, only one smoothing length level was used in these simulations. The agreement with the analytical solution, plotted with a solid line, is seen to increase with the increasing particle number n used in the simulations. Both with a choice of $n = 800$ and $n = 400$, the velocity and density are well represented by the simulations, whereas the pressure
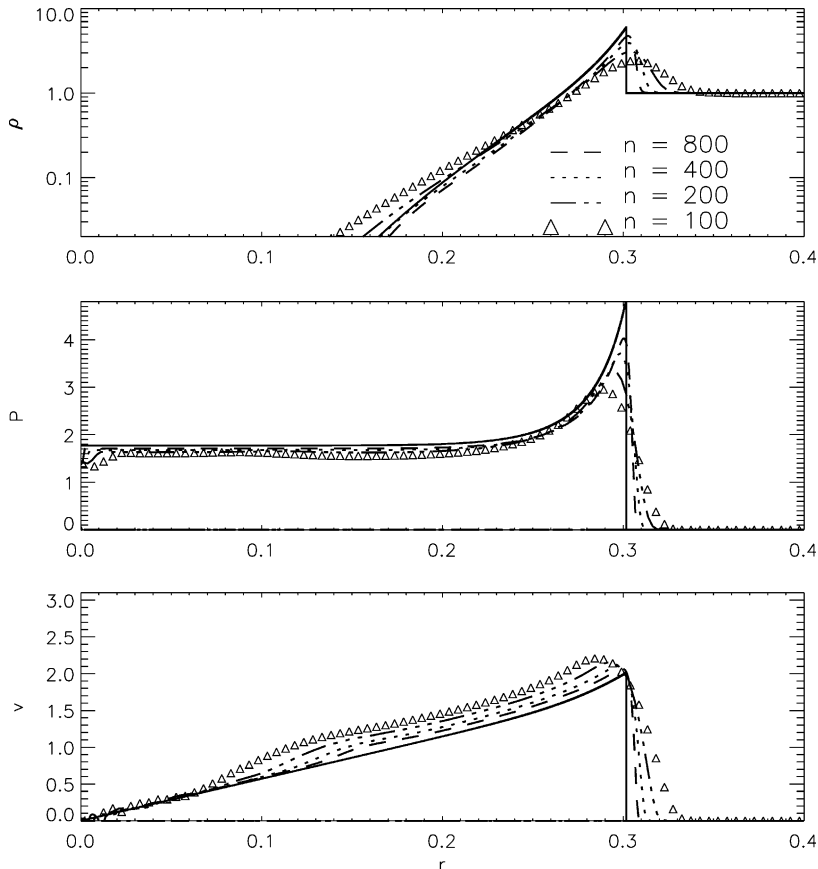

Fig. 6. Sedov blast wave test at $t = 0.05$ for density, pressure and velocity in a spherically symmetric system.

level is somewhat underestimated. In the current simulations, the balloon radius was set to $r_0 = 0.025$. As was illustrated in Eq. (32), the bursting balloon analogue is only an approximation to the point explosion problem. The results are therefore dependent on the choice of balloon radius. It is found that an increase in the balloon volume leads to a better fit of the numerical velocity profile to the analytical velocity solution, but it also leads to a shift in the shock front, and consequently results in a poorer fit of the density and pressure profile compared to the Sedov point explosion solution. Reducing the balloon radius, leads to a small shift to the left in the density, pressure and velocity profile. This leads to a poorer fit of the velocity profile to the analytical solution.

5. Planar symmetry

The formulation as described for the spherically symmetric problem, is also applicable to planar symmetry. For a planar symmetric case, $F(\mathbf{r}) = F(z)$, the integral interpolant reduces to

$$\langle F(z) \rangle = \int \mathrm{d}z' \, F(z') \int_{|z'-z|/h}^{2} \mathrm{d}q \, 2\pi h^2 q \mathscr{W}_3(q) \tag{33}$$

$$\equiv \int \mathrm{d}z' F(z') W_{3P1}(z', z; h), \tag{34}$$

where

$$W_{3P1}(z', z; h) = \frac{1}{h} \begin{cases} \frac{7}{10} - C(|\sigma' - \sigma|), & 0 \leqslant |\sigma' - \sigma| < 1, \\ \frac{8}{10} - D(|\sigma' - \sigma|), & 1 \leqslant |\sigma' - \sigma| < 2, \end{cases} \tag{35}$$

with $\sigma' \equiv z'/h$ and $\sigma \equiv z/h$. In the planar case, with $W_{3P1} \equiv W_{3P1}(z_i, z_j; h)$, we have $\partial W_{3P1}/\partial z' = -\partial W_{3P1}/\partial z$ as expected. The equations of motion thus take the familiar form

$$\frac{\mathrm{d}z_i}{\mathrm{d}t} = v_i, \tag{36}$$

$$\rho_i = \sum_j m_j W_{3P1}, \tag{37}$$

$$\frac{\mathrm{d}v_i}{\mathrm{d}t} = -\sum_j m_j \left(\frac{P_i}{\rho_i^2} + \frac{P_j}{\rho_j^2} + \pi_{ij} \right) \frac{\partial}{\partial z_i} W_{3P1}, \tag{38}$$

$$\frac{\mathrm{d}e_i}{\mathrm{d}t} = \sum_j m_j \left(\frac{P_i}{\rho_i^2} + \frac{1}{2} \pi_{ij} \right) v_{ij} \frac{\partial}{\partial z_i} W_{3P1}, \tag{39}$$

$$P_i = (\gamma - 1) e_i \rho_i. \tag{40}$$

In the planar case, m_j is the mass inside a plane parallel slab with sides of unit length and thickness dz, whereas $v_{ij} = v_i - v_j$.

Cartesian problems in 1D have traditionally been studied with a 1D version of the kernel function equation (2),

$$W_1(z', z; h) = \mathscr{W}_1(q), \tag{41}$$

with $q = |z' - z|/h$. It is therefore of some interest to compare numerical results based on W_{3P1} and W_1. In Fig. 7, we show the relative numerical error of the homogeneous planar compression problem with W_{3P1} (thick lines) and W_1 (thin lines) as kernel functions, given $v_z = -z$. The figure illustrates that the relative amplitude error of ρ (solid lines) and e (dash-dotted lines) are significantly larger when the W_1 kernel function is used. As in the spherical case, we observe that the relative error is reduced as the interparticle distances are reduced.

The Sod problem [9] has also been tested for the planar case and the results are presented in Fig. 8. Density, pressure, internal energy and velocity are plotted as functions of position at $t = 0.5$. The time is defined relative
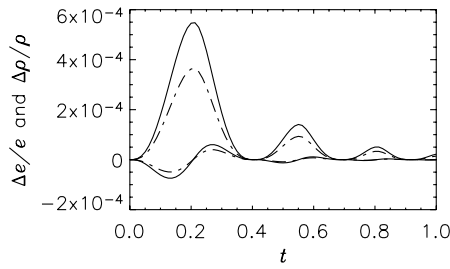
Fig. 7. Relative error in the density (solid lines) and energy (dash-dotted lines) for a controlled planar compression. Thin lines and thick line represent results obtained with the W_1 and W_{3P1} as kernel functions, respectively.
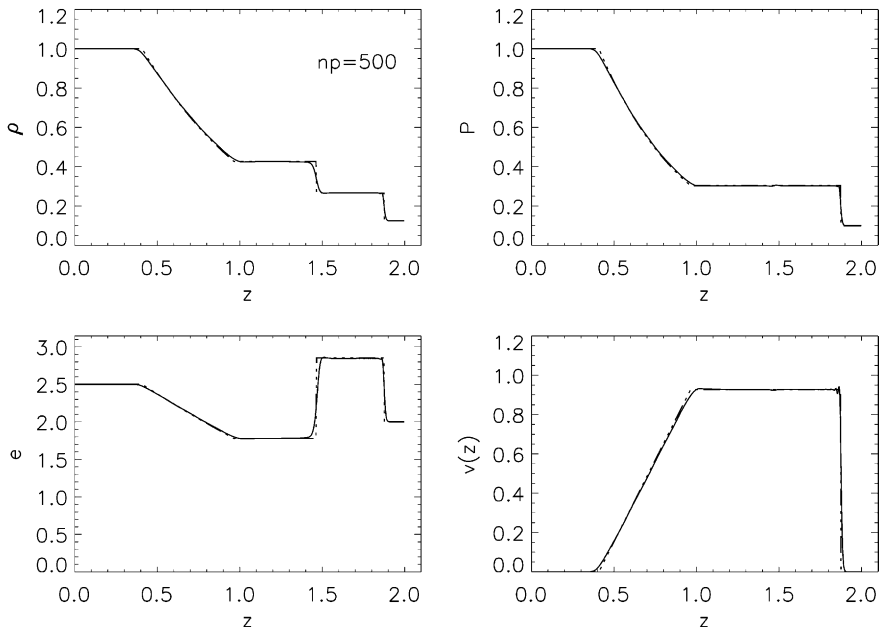

Fig. 8. Shock tube test in Cartesian coordinates at $t = 0.5$. Solid lines show the results obtained with RSPH and dashed lines show the analytical results.

to the removal of the membrane at the location $z = 1$. When the numerical results (solid lines) are compared to the analytical solution (dashed lines), the agreement is good, as the two curves are difficult to distinguish. This also applies close to origin. In this planar case, reflecting boundary conditions were used on both boundaries. The particle number in these simulations was 500.

The Noh test [6] has also been performed in the planar case, with the same initial conditions as for the spherical coordinate system. The post-shock conditions, however, differ. In the planar case, the analytical post-shock conditions are $\rho_+ = 4$, $v_+ = 0$, $p_+ = 4/3$ and $e_+ = 1/2$. Once more the shock position is given as $R_s = t/3$. In Fig. 9, the results for the planar case is presented for density, pressure, internal energy and velocity. The numerical results are plotted using solid lines, whereas the analytical solution is plotted with dashed lines. In the present simulations, the initial particle number was 2000 while approximately 800 particles remain at $t = 0.6$. The agreement with the analytical results is good, except for the region close to origin. As discussed for the spherical case, the density dip and energy rise near the symmetry plane $z = 0$ are problems related to the shortcomings of the artificial viscosity [19]. Here, no attempt was made to correct for this phenomena.
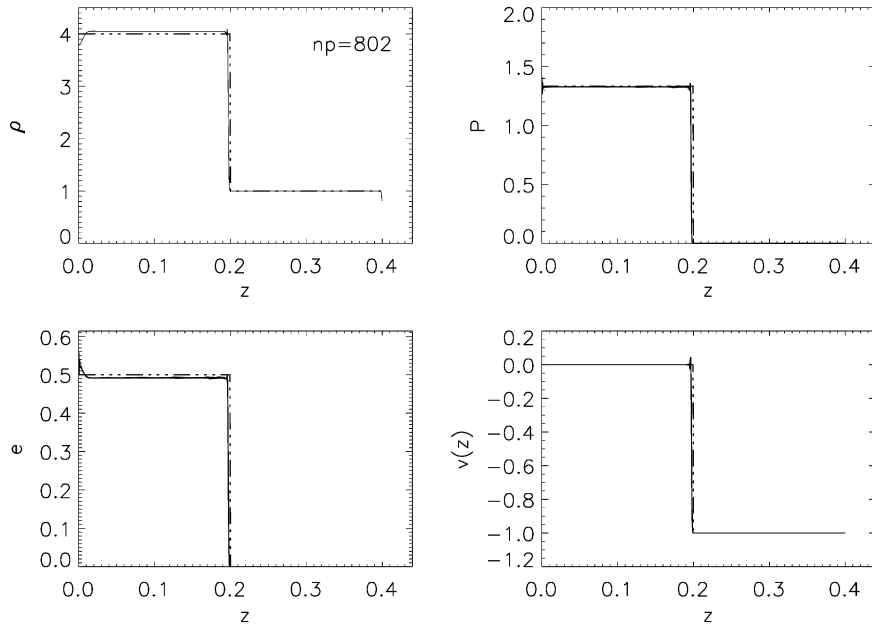
Fig. 9. Nohs numerical test for Cartesian coordinates at $t = 0.6$. Solid lines show results obtained with RSPH and dashed lines show the analytical results.

6. Cylindrical symmetry

The procedure used for the spherically symmetric case can easily be extended also to cylindrically symmetric systems. In the cylindrical case, the expression for the integral interpolant reduces to

$$\langle F(r,z) \rangle = \int dr' \, r' \, dz' \, F(r',z') \int d\varphi \, \mathscr{W}_3(q)$$

$$\equiv \int dr'r'dz'F(r',z')W_{3C2}(r',z',r,z;h), \tag{42}$$

where $q = \sqrt{(z'-z)^2 + (r'-r)^2 + 4r'r\sin^2(\varphi/2)}/h$. The kernel function for cylindrical symmetry is thus given as

$$W_{3C2}(r',z',r,z;h) = 4 \int_0^{\arcsin(\min(1,\sqrt{(4-A)/B}))} \mathscr{W}_3\left(\sqrt{A + B\sin^2 v}\right) dv. \tag{43}$$

In Eq. (43), we defined $A = ((z'-z)^2 + (r'-r)^2)/h^2$ and $B = 4r'r/h^2$. Unfortunately, the kernel function and its derivatives are this time expressed in terms of elliptic integrals. In SPH applications, it is imperative that the kernel function and its derivatives can be evaluated fast. For the present case, it thus seems necessary to make use of numerical evaluation by table interpolation. For cylindrical symmetry with $W_{3C2} \equiv W_{3C2}(r_j,z_j,r_i, z_i;h)$, we find $\partial W_{3C2}/\partial z' = -\partial W_{3C2}/\partial z$ while, similarly to the spherical case, $\partial W_{3C2}/\partial r' \neq -\partial W_{3C2}/\partial r$.

The 2D kernel function W_{3C2} is only one of several alternative kernel functions for cylindrical symmetry. Another choice is W_{5PC2}, where the notation indicates that the dimension, (δ), of the "generic" kernel function $\mathscr{W}_\delta$ has been reduced from 5 to 3 through a "planar symmetric" transformation (P), and then to 2 by a cylindrically symmetric transformation (C). Correspondingly, in the 1D cylindrically symmetric case, two alternative forms are W_{2C1} and W_{4PC1}. We note that W_{3C2}, W_{2C1}, W_{5PC2} and W_{4PC1} all have identical range in $r' - r$. The former set of kernel functions are $\mathscr{C}^2$-continuous, whereas the latter set are $\mathscr{C}^3$-continuous. Making use of W_{3C2}, the equations of motion for the cylindrically symmetric case are

$$\frac{dr_i}{dt} = v_{ri}, \tag{44}$$

$$\frac{dz_i}{dt} = v_{zi}, \tag{45}$$

$$\rho_i = \sum_j m_j W_{3C2} \tag{46}$$

$$\frac{dv_{ri}}{dt} = -\sum_j m_j \left(\frac{P_i}{\rho_i^2} + \frac{P_j}{\rho_j^2} + \Pi_{ij} \right) \frac{\partial}{\partial r_i} W_{3C2}, \tag{47}$$

$$\frac{dv_{zi}}{dt} = -\sum_j m_j \left(\frac{P_i}{\rho_i^2} + \frac{P_j}{\rho_j^2} + \Pi_{ij} \right) \frac{\partial}{\partial z_i} W_{3C2}, \tag{48}$$

$$\frac{de_i}{dt} = \sum_j m_j \left(\frac{P_i}{\rho_i^2} + \frac{1}{2} \Pi_{ij} \right) \left(v_{rj} \frac{\partial}{\partial r_j} + v_{ri} \frac{\partial}{\partial r_i} + v_{zij} \frac{\partial}{\partial z_i} \right) W_{3C2}, \tag{49}$$

$$P_i = (\gamma - 1)e_i \rho_i. \tag{50}$$

Here, m_j is, apart from a factor 2π, the mass inside a cylindrical shell of radius r_j, thickness dr and length dz. The identical set of equations applies if W_{3C2} is replaced by W_{5PC2}.

6.1. Simple cylindrical test cases

The relative error of a controlled cylindrical compression test with $v_z = 0$ and $v_r = -r$ is presented in Fig. 10. Here the relative errors of $\Delta\rho/\rho$ (solid lines) and $\Delta e/e$ (dash-dotted lines) resulting from Eqs. (46) and (49) as compared with the analytical results are displayed, using the 1D kernel functions W_{2C1} (thin lines) and W_{4PC1} (thick lines). Note that the relative error of e with kernel function W_{2C1} has been multiplied by 1/100. It thus appears that a significant numerical improvement is achieved by making use of the higher order continuous kernel function W_{4PC1}. Similar improvements are expected for the 2D case, that is, making use of W_{5PC2} instead of W_{3C2}.

In Fig. 11, we present the RSPH (dotted lines that look like solid lines) and Riemann solver (dashed lines) solutions for a cylindrically symmetric version of the Sod problem [9]. The problem was run with a 2D code, with the membrane initially positioned at an axial distance $r = 1$. The total number of particles in the computational domain ($0 < r < 2$, $0 < z < 0.5$) was 40,000. No additional smoothing is used in the presentation of these data, as we make a projection of particles found within the layer $0.2 < z < 0.3$ on to the r–t plane. Consequently, each point in Fig. 11 is the position and value of individual particles. Again the results are in good agreement with the results of the Riemann solver.

The analytical solution to the corresponding Noh test [6] is different from both the planar and spherical case although the initial conditions are the same. The post-shock conditions are $\rho_+ = 16$, $v_+ = 0$, $p_+ = 16/3$ and $e_+ = 1/2$, while the pre-shock density given as a function of radius is $\rho_- = (1 + t/r)$. As in the previous cases, the shock position is given as $R_s = t/3$, consequently, at the shock front position R_s, the post-shock density is
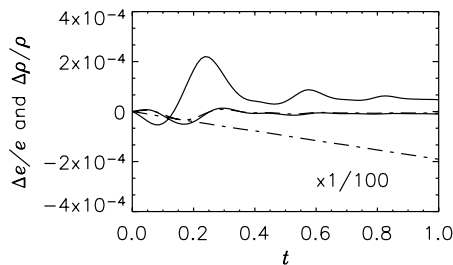

Fig. 10. Relative error in density (solid lines) and energy (dash-dotted lines) for a controlled cylindrical compression. Thin lines represent results obtained with W_{2C1}, thick lines W_{4PC1}.
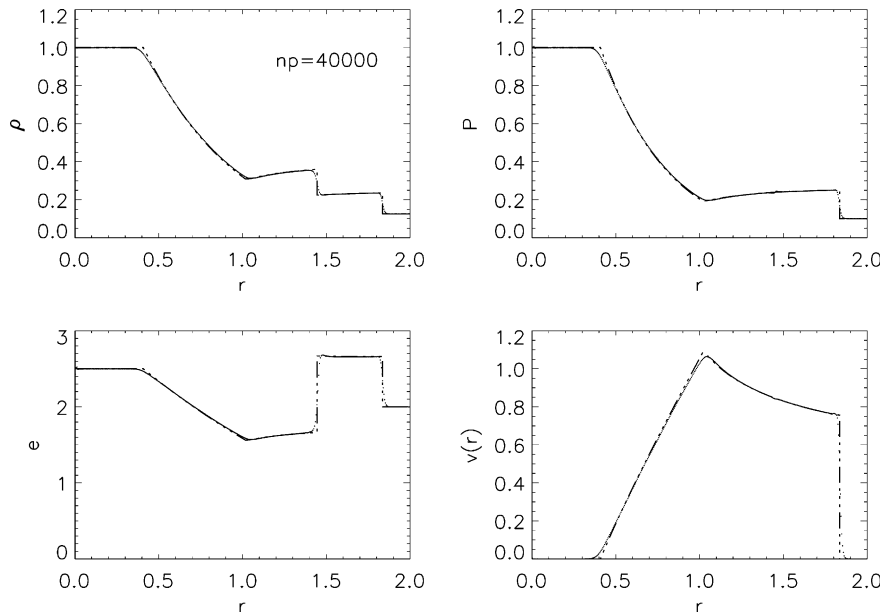
Fig. 11. Sod numerical test for a 2D cylindrical code at $t = 0.5$. Dotted lines show the results obtained with RSPH and dashed lines show the results with a Riemann solver code.

constant $\rho = 4$. The results for the density, pressure, internal energy and radial velocity are plotted in Fig. 12 with solid lines for the numerical results, and dashed lines for the analytical results. As discussed in the spherical case, the agreement is good, except for the region close to origin, where the excess wall heating problem gives rise to a density dip and an internal energy rise.
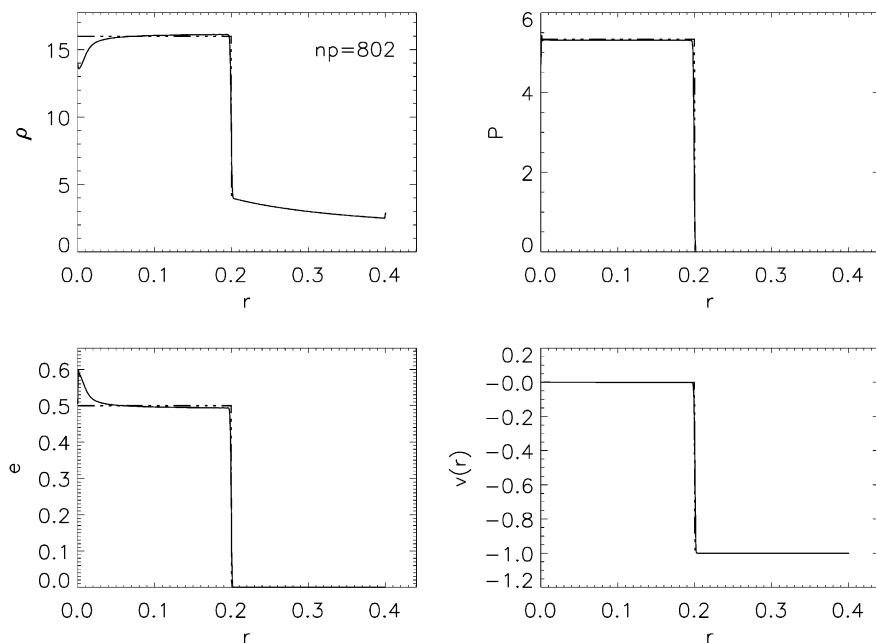

Fig. 12. Noh numerical test for a cylindrically symmetric system at $t = 0.6$. Solid lines show the results obtained with RSPH and dashed lines show the analytical results.
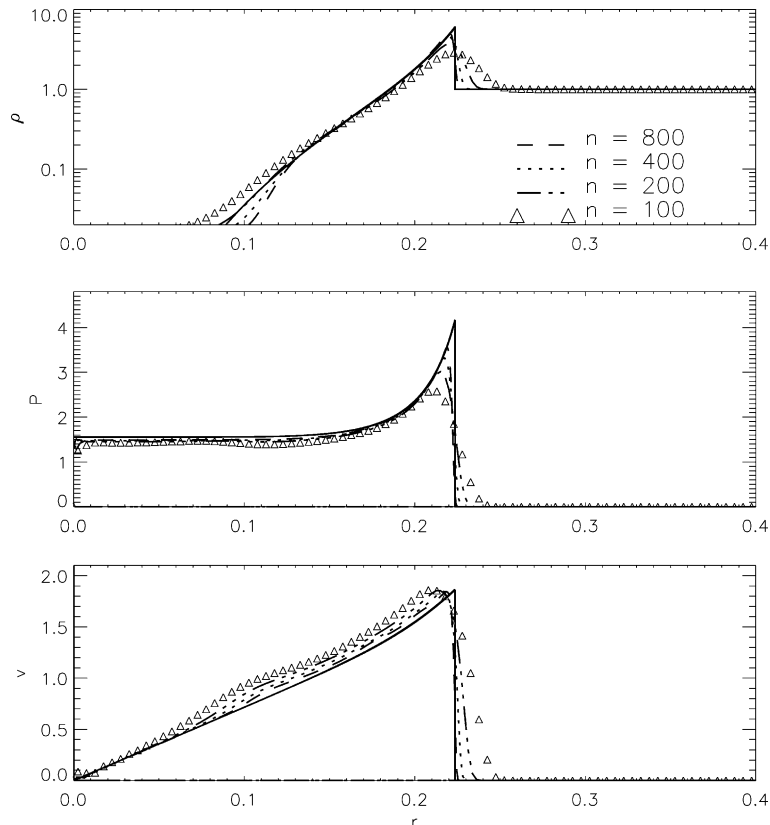
Fig. 13. Sedov blast wave test at $t = 0.05$ for density, pressure and velocity in a cylindrically symmetric system.

The point explosion test introduced by Sedov [26] is also studied for a cylindrical system. Inside the balloon, pressure is chosen in accordance with Eq. (32) with $\delta = 2$. The results are presented in Fig. 13 for the density, pressure and velocity. The analytical solution is plotted with a solid line. As the smoothing length is reduced, the particle number increases, and the fit to the analytical solution is improved. The density and velocity levels are well represented by the numerical simulations, the pressure peak, however, is slightly underestimated. Only one smoothing length level was used in these simulations.

The numerical simulations are based on the assumption that the point source explosion can be represented by a pressurized balloon of finite volume. In these simulations, we have chosen a balloon radius $r_0 = 0.015$. We find that a reduction of the balloon volume leads to a left-hand shift in the pressure, density and velocity profile, and similarly, an increased volume leads to a right-hand shift of the profiles. The best fit to the analytical pressure solution was found for $r_0 = 0.03$, where the levels are comparable. The velocity profile, however, gave a poorer fit to the analytical solution in this case.

7. Spherical shock interactions in cylindrical symmetry

Except for the cylindrical Sod test, the results presented so far have all been one dimensional, and for simplicity we have used a constant smoothing length in all simulations. In our last example, we wish to study a fully 3D problem, first presented in Section 7.1 with a constant smoothing length. Finally, in Section 7.2, we demonstrate the full capability of the symmetric formulation with RSPH, allowing the smoothing length to vary in a piecewise constant manner. The resolution is optimized by performing particle regularization at regular time intervals.

We look at a cylindrically symmetric blast wave problem in which two spherical balloons of equal radii, centered at the symmetry axis are given high pressure and density relative to the surrounding medium. The

$\gamma = 1.4$ gas of the balloons are initially at rest, separated from the surrounding by spherical membranes. When the membranes are removed, the pressure and density differences cause two individually spherical shocks to be formed. The initial conditions are given as follows:

$$P = \begin{cases} 10^4, & \sqrt{r^2 + (z-4)^2} < 0.5, \\ 10^3, & \sqrt{r^2 + (z-6)^2} < 0.5, \\ 10^{-2}, & \text{otherwise} \end{cases} \tag{51}$$

and

$$\rho = \begin{cases} 10, & \sqrt{r^2 + (z-4)^2} < 0.5, \\ 10, & \sqrt{r^2 + (z-6)^2} < 0.5, \\ 1.0, & \text{otherwise.} \end{cases} \tag{52}$$

A computational domain of $(r, z) = \{[0, 4], [0, 9]\}$ are used for the current simulations.

7.1. Results with a constant smoothing length

In Fig. 14, density profiles in the r–z plane are presented for different times with a color-bar on the right-hand side indicating the density levels. The figure shows the formation and collision of two spherical shocks. Since the higher pressure jump will generate a faster moving shock, the two shocks of Fig. 14(a) are observed to have different radii. In both cases, rarefaction waves are moving inwards, reducing the pressure and density inside the originally high pressure regions. The density difference inside the two shocks are illustrated by the difference in colors. At $t = 0.02$, the two shocks in Fig. 14(a) are about to collide, with their point of contact still at the symmetry axis. Later, at $t = 0.04$, the point of contact has left the symmetry axis. The highest density area, here plotted in white, is observed where the two shock fronts meet in Fig. 14(b). The collision of the two shocks generates reflected shocks traveling in opposing directions relative to the initial shocks. The reflected shock of the lower balloon is most clearly observed moving downwards, causing the inner region of the lower balloon to look asymmetric. The reflected wave continues to propagate downwards as Fig. 14(c) illustrates, whereas the reflection point moves outwards. For the consecutive time step $t = 0.1$ and $t = 0.14$, the density inside the two balloons are gradually smoothed, and the reflected pattern of the two shock fronts towards the symmetry axis are becoming less apparent. An enlargement of the interaction region of the two shocks is shown in Fig. 14(f) for $t = 0.14$.

The complex shock reflection and interaction pattern obtained when the two shocks collided are further illustrated in Fig. 15(a), where the absolute velocity for $t = 0.14$ has been plotted. The initial spherical shock fronts and shock interaction points are easily recognized. In comparison with the density plot of Fig. 14(e) the distinct appearance of the curved reflected shock is also worth noting.

Fig. 15(b) shows the density profile parallel to the symmetry axis, plotted for different radial distances. The solid line is used for $r = 0.05$, the dotted line for $r = 1.0$, and the dashed line for $r = 1.64$. The shock fronts are distinct, with little or no noise visible. The highest density level is observed in the shock interaction area, for $r = 1.64$. In the present simulations, we allow particle regularization, but keep the smoothing length constant, $h = 0.0265$. With 1.7 particles per h, 1.5×10^5 particles are used in these computations.

7.2. Results with a variable resolution using RSPH

We also study the collision of two spherical shocks allowing a variable resolution in our computations, through the use of a piecewise constant smoothing length. The density profile for this case is given in Fig. 16. The shock front and shock interaction point are distinct and well resolved. In comparison with Fig. 14, Fig. 16 illustrates how the improved resolution leads to a reduction in the shock front width, and an increase in the density level at the shock interaction point.
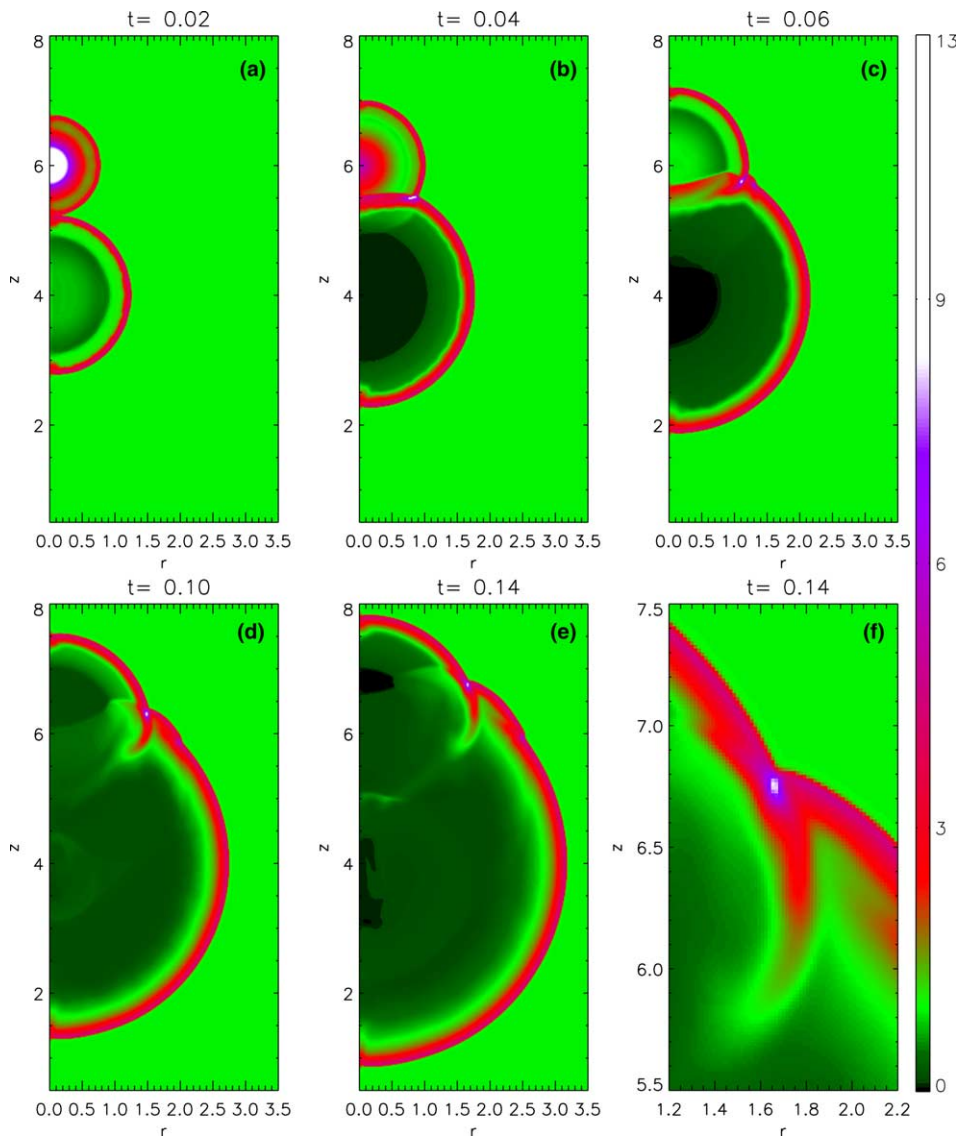
Fig. 14. Density profiles for the cylindrical blast wave test at: (a) $t = 0.02$, (b) $t = 0.04$, (c) $t = 0.06$, (d) $t = 0.1$ and (e) $t = 0.14$. (f) An enlargement of the shock interaction point at $t = 0.14$.

In these simulations, we use 1.7 particles per h. The maximum smoothing length was set to $h = 0.34$, and we allow for 6 smoothing lengths levels. The h-profile is determined from the density and velocity gradients in the current simulation, and is only modified when regularization is performed. Fig. 17(a) illustrates the smoothing length profile at $t = 0.14$. As the colorbar shows, the darker the color is, the finer is the resolution. If the h-profile is compared with the density plot in Fig. 16(e) and the absolute velocity plot in Fig. 17(b), it is clear that the fine resolution is used for most of the shock structures, whereas the smoothing length is increased in areas where there is less or no dynamics. Note that the fine resolution is not restricted to the high density regions, as would be the case with standard SPH [29], but is also found in the rarefied regions with high velocities. Comparing the velocity profiles of Figs. 15(a) and 17(b) illustrate how the introduction of a variable smoothing length profile has improved the resolution and the level of details observed. The smoothing length algorithm is constructed so that the smoothing length profile only varies in steps of two, as illustrated in Fig. 17(a). Particle regularization ensures that the smoothing length profile is optimized at regular time intervals. In
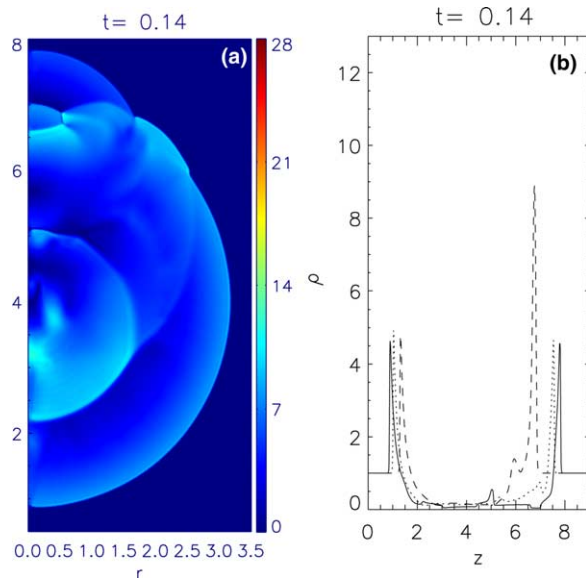
Fig. 15. (a) Absolute velocity at $t = 0.14$. (b) Density profiles at $r = 0.05$, 1.0 and 1.64 are plotted with solid, dotted and dashed lines, respectively.

the current simulations, the average number of particles used is approximately 1.5×10^5, which is about the same number of particles used for the constant h simulations. The number of particles necessary to obtain comparable resolution with a constant smoothing length would be approximately 9.2×10^5 particles.

In Fig. 17(c), the density profiles parallel to the symmetry axis have been plotted for the radial distances of $r = 0.05$, 1.0 and 1.64 with solid, dotted, and dashed lines, respectively. The density peaks are well resolved and, in comparison with Fig. 15(b) we observe an increase in the density peak values, most prominent for the dashed line crossing the shock interaction point. This is due to the increased resolution obtained with the introduction of a step-wise variable smoothing length, which serves to improve the capturing of density and pressure discontinuities.

The results presented illustrate how the use of multiple smoothing length levels combined with regularization produce high quality results with relatively low particle numbers. In spherical and cylindrical symmetry, the numerical discretization error is found to increase towards the origin or the symmetry axis, respectively. In these simulations, auxiliary particles, described in closer details in [12], have been used to reduce this problem within a $2h$ smoothing length distance from the axis. See Section 8 for a detailed discussion of this.

8. Discussion

The development of 3D SPH codes in Cartesian coordinates is straight forward. The number of interpolation particles in such 3D computations are, however, restricted by computer resources. Special formulation of SPH codes for spherically and cylindrically symmetric systems therefore still have interest, and a wide range of applications. Examples in astrophysics are the formation of bow shocks, phenomena in the solar atmosphere, the formation of accretion disks, and black holes. In material modeling, impact studies have been performed with an axi-symmetric assumption, and so has the source description in blast wave studies.

This work was initiated after facing the short-comings of the technique suggested in [8] in the region close to the symmetry axis, for a cylindrically symmetric system. Going back to the basic interpolation theory of the SPH method we have developed new kernel functions that reflect the assumed symmetry of the problem. A Lagrangian formalism was further used to develop new sets of equations of motion in the proper coordinate system. In contrast to previous descriptions the equations of motion are no longer singular at the point/axis of symmetry $r = 0$. Furthermore, the new kernel function formulations embed the natural boundary conditions
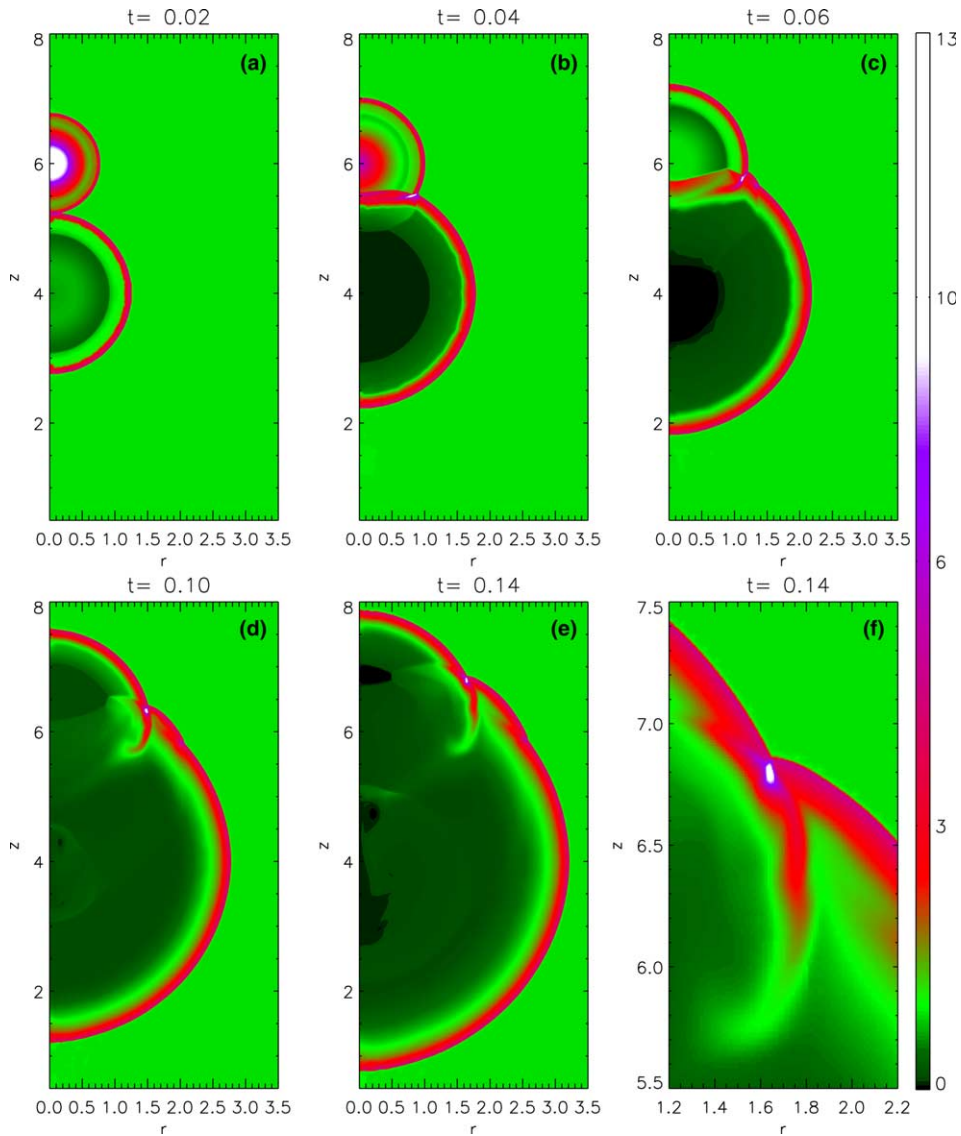
Fig. 16. Density profiles for the cylindrical blast wave test at: (a) $t = 0.02$, (b) $t = 0.04$, (c) $t = 0.06$, (d) $t = 0.1$ and (e) $t = 0.14$. (f) An enlargement of the shock interaction point at $t = 0.14$.

at $r = 0$ in both the spherically symmetric and cylindrically symmetric case. Additional boundary conditions at $r = 0$ are therefore not needed.

The cylindrical version of the Sod shock tube test was studied in [8]. Due to the problems at the symmetry axis, the membrane was positioned and results only presented in a region well separated from $r = 0$. The results presented with the current technique indicate a significantly improved treatment near the axis, and the overall agreement with numerical results from a Riemann solver is good. In [5] results of the spherical Noh problem with a 2D cylindrical SPH code was presented. Deviations in their results from the analytical solution can be seen, at both the inner and outer boundaries. Additionally, the solution fails to reproduce the correct shock position and post-shock density level. The solution to the Noh problem was improved in [7] by introducing a set of additional stress points in the SPH formulation. Although the formulation does not seem to reproduce the exact analytical density level, the improvements are pronounced, as the shock position and the pre-shock shape give better agreement with the analytical solution. In our new formulation of SPH with
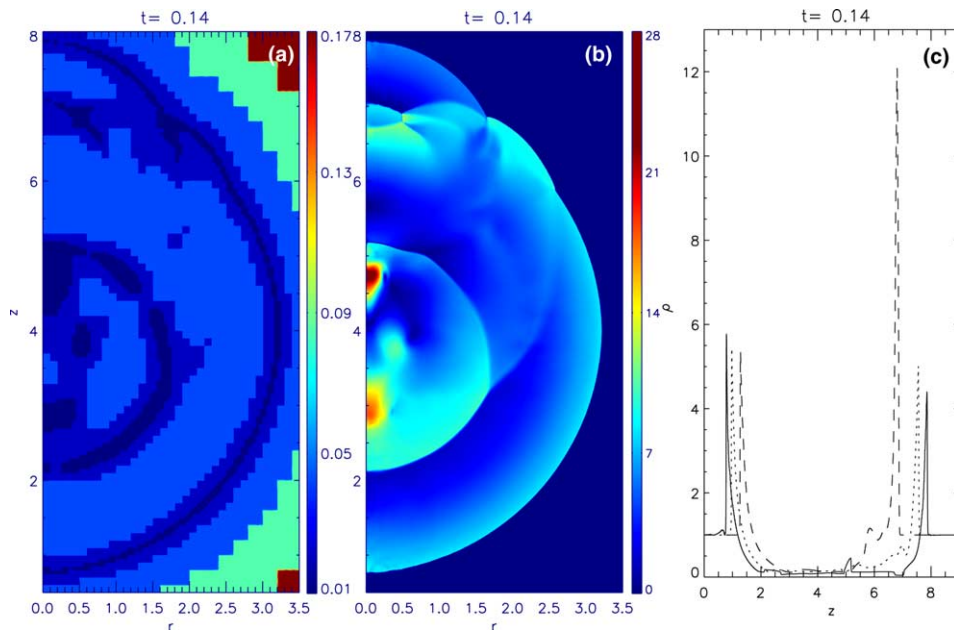
Fig. 17. (a) The smoothing length profile h and (b) absolute velocity at $t = 0.14$. (c) The density profiles at $r = 0.05$, 1.0 and 1.64 are plotted with solid, dotted and dashed lines, respectively.

symmetries, the analytical solutions are reproduced to high accuracy in both the spherical, the cylindrical, and the planar case of the Noh infinite shock problem. The excess wall heating problem [6] was not addressed in any of the results reported, but our results demonstrate that the problem is observed independently of the coordinate system chosen, and will according to [6] be mended through the introduction of artificial heat conduction. The problem is related to the formulation of the artificial viscosity.

The Sedov point explosion problem was simulated making use of the bursting balloon analogue, similar to the numerical setup used by Fryxell et al. in their adaptive mesh refinement hydrodynamic code [30]. In the cylindrical case our results for the two finest smoothing lengths are comparable to their 2D simulation with 8 levels of mesh refinement. As in our results, their density and velocity profiles are well fitted with the analytical solutions. Their pressure level is slightly under-estimated, however, as was also observed in our results. In [30] the 2D simulations were performed in a Cartesian coordinate system, a radial averaging technique was therefore applied on the plotted results. Our results are presented without any kind of smoothing. Fryxell et al. [30] also presented 3D results of the spherical Sedov problem. The results are again averaged, and rather large error estimates are included in the presentation. Their results are presented using 5 levels of mesh refinement. In these results the peak values are clearly underestimated, especially for the pressure. Our SPH results are slightly better, even for a low resolution run of 200 particles with one smoothing length level.

The Sedov point explosion problem has also been studied with traditional and adaptive (A)SPH methods by Owen et al. [11]. They do not take advantage of the symmetry in the problem, as their results are presented in 2D and 3D Cartesian coordinates. The initialization of the problem is slightly different from that of the balloon analogue, and the simulations are presented within a smoothing length range $h = [1.0 \times 10^{-5}, 0.12]$. Although the results are presented for slightly different time steps, it is clear that their 2D simulations of the density is under-estimated both for the traditional and adaptive SPH. Also the shock front is shifted to the right compared with the analytical solution. This may be due to the choice of initialization of the problem. Owen et al. also performed 3D simulations with coarser resolution. We find that our 100 particles simulation shows better agreement with the analytical solution, than those presented by [11] using 32^3 particles. For the chosen time step $t = 0.1$, their pressure and velocity post shock profiles show significant deviation from the analytical solution.

The numerical SPH formulation presented in this paper should be independent of the method chosen for allowing variations in the smoothing length. Most of the results presented here were therefore performed with a constant smoothing length. In our final example, however, the new formulation is applied to a more realistic situation, using the full capability of our RSPH code, as we study the collision of two spherical shocks in cylindrical symmetry. For this result the smoothing length is allowed to vary in a piecewise constant manner, allowing for $6h$-profile levels and the resolution is optimized through the use particle regularization at regular time intervals. The results are compared with the results of a constant smoothing length simulation, and demonstrate high resolution of the shock structures, and a fine-structured smoothing length profile, obtained with a relatively low particle number.

In spherical and cylindrical symmetry the numerical discretization error in the process of replacing the integral interpolant with a discrete summation interpolant will increase towards the origin or symmetry axis, respectively. This is a consequence of the particular shape of the kernel function required by the assumed symmetry in this region. In the original SPH formulation this problem can be handled by decreasing the interparticle distance in this area, in a manner similar to what was discussed for the Sod test in Section 4, when regularization was not applied. In RSPH, the performance of the discrete formulation is improved by using auxiliary particles within a $2h$ distance from the symmetry axis. The auxiliary particles were originally introduced in RSPH to handle the area near steps in the smoothing length. The details of this method is discussed in closer details in [12].

A concluding remark on kernel functions may be appropriate. The success of an SPH formalism that is to reflect a particular problem symmetry rests on the development of proper kernel functions that incorporate that symmetry. At the same time the efficiency of the SPH code depends on the efficiency in evaluating this kernel function and its derivatives. For spherical or planar symmetry the derived kernel functions were expressed in simple analytical forms. In the case of cylindrical symmetry, however, the analytical form of the corresponding kernel function, derived on the basis of the standard third order B-spline function, is expressed in terms of elliptic functions. Efficiency in this case thus requires the kernel function and its derivatives to be evaluated through table interpolation. Work is currently in progress to implement alternative kernel functions for the cylindrical case with equal or improved performance that allows for fast and direct evaluation.

References

[1] R.F. Stellingwerf, Smooth particle hydrodynamics, Lect. Notes Phys. 395 (1991) 239–246.
[2] M. Herant, W. Benz, Postexplosion hydrodynamics of sn 1987a, Astrophys. J. 387 (1992) 294–308.
[3] C.S. Coleman, G.V. Bicknell, Jets with entrained clouds. Hydrodynamic simulations and magnetic field structure, Mon. Not. R. Astron. 214 (1985) 337–355.
[4] D. Molteni, H. Sponholz, Formulation of the SPH method for axially symmetric problems: simulations of accretion disks, Mem. S.A. It. 65 (1994) 1183–1191.
[5] A.G. Petschek, L.D. Libersky, Cylindrical smoothed particle hydrodynamics, J. Comput. Phys. 109 (1993) 76–83.
[6] W.F. Noh, Errors for the calculations of strong shocks using an artificial viscosity and an artificial heat flux, J. Comput. Phys. 72 (1987) 78–120.
[7] P.W. Randles, L.D. Libersky, Normalized SPH with stress points, Int. J. Numer. Methods Eng. 48 (2000) 1445–1462.
[8] L. Brookshaw, Smooth particle hydrodynamics in cylindrical coordinates, ANZIAM J. 44 (2003) C114–C139.
[9] A. Sod, A survey of several finite difference methods for systems of nonlinear hyperbolic conservation laws, J. Comput. Phys. 27 (1978) 1–31.
[10] M.B. Liu, G.R. Liu, K.Y. Lam, Constructing smoothing functions in smoothed particle hydrodynamics with applications, J. Comput. Appl. Math. 155 (2003) 263–284.
[11] J.M. Owen, J.V. Villumsen, P.R. Shapiro, H. Martel, Adaptive smoothed particle hydrodynamics: Methodology ii, Astrophys. J. Suppl. Series 116 (1998) 155–209.
[12] S. Børve, M. Omang, J. Trulsen, Regularized smoothed particle hydrodynamics with improved multi-resolution handling, J. Comput. Phys. 208 (2005) 345–367.
[13] J.J. Monaghan, Smoothed particle hydrodynamics, Annu. Rev. Astrophys. 30 (1992) 343–374.
[14] J.J. Monaghan, J.C. Lattanzio, A refined particle method for astrophysical problems, Astron. Astrophys. 149 (1985) 135–143.
[15] J.J. Monaghan, On the problem of penetration in particle methods, J. Comput. Phys. 82 (1) (1989) 1–15.
[16] C. Eckert, Variation principles of hydrodynamics, Phys. Fluids 3 (1960) 421–427.
[17] J.J. Monaghan, D.J. Price, Variational principles for relativistic smoothed particle hydrodynamics, Mon. Not. R. Astron. 328 (2001) 381–392.
[18] S. Inutsuka, Reformulation of smoothed particle hydrodynamics with Riemann solver, J. Comput. Phys. 179 (1) (2002) 238–267.

[19] J.V. Neumann, R.D. Richtmyer, A method for the numerical calculation hydrodynamic shocks, J. Appl. Phys. 21 (1950) 232–237.

[20] S. Børve, A numerical study of ionospheric and magnetospheric phenomena using particle simulation techniques, Ph.D. thesis, Faculty of Mathematics and Natural Science, University of Oslo, 2001.

[21] S. Børve, M. Omang, J. Trulsen, 2d regularized smoothed particle hydrodynamics mhd stability analysis, Astrophys. J. Suppl. Series 153 (2004) 447–462.

[22] M. Omang, S. Børve, J. Trulsen, Numerical simulation of shock wave phenomena using smoothed particle hydrodynamics, in: Proceedings of the 14th the International Mach Reflection Symposium, 2000, pp. 181–192.

[23] M. Omang, S. Børve, J. Trulsen, Numerical simulations of shock-vortex interaction using regularized smoothed particle hydrodynamics, Comput. Fluid Dyn. J. 12 (2003) 258–265.

[24] S. Børve, M. Omang, J. Trulsen, Regularized smoothed particle hydrodynamics: a new approach to simulating magnetohydrodynamic shocks, Astrophys. J. 561 (2001) 82–93.

[25] J.J. Monaghan, R.A. Gingold, Shock simulations by the particle method SPH, J. Comput. Phys. 52 (1983) 374–389.

[26] L.I. Sedov, Similarity and Dimensional Methods in Mechanics, Academic Press Inc, London, 1959, p. 210 (Chapter 11).

[27] H.L. Brode, Numerical solutions of spherical blast waves, J. Appl. Phys. 26 (1955) 766–775.

[28] H.L. Brode, Blast wave from a spherical charge, Phys. Fluids 2 (1959) 217–229.

[29] W.S.D.V. Springel, N. Yoshida, Gadget: a code for collisionless and gasdynamical cosmological simulations, New Astron. 6 (2001) 79.

[30] B. Fryxell, K. Olson, P. Picker, F.X. Timmes, M. Zingale, D.Q. Lamb, P. MacNeice, R. Rosner, J.W. Truran, H. Tufo, Flash: An adaptive mesh hydrodynamics code for modeling astrophysical thermonuclear flashes, Astrophys. J. Suppl. S. 131 (2000) 273–334.